

PCCP

Accepted Manuscript



This is an *Accepted Manuscript*, which has been through the Royal Society of Chemistry peer review process and has been accepted for publication.

Accepted Manuscripts are published online shortly after acceptance, before technical editing, formatting and proof reading. Using this free service, authors can make their results available to the community, in citable form, before we publish the edited article. We will replace this *Accepted Manuscript* with the edited and formatted *Advance Article* as soon as it is available.

You can find more information about *Accepted Manuscripts* in the [Information for Authors](#).

Please note that technical editing may introduce minor changes to the text and/or graphics, which may alter content. The journal's standard [Terms & Conditions](#) and the [Ethical guidelines](#) still apply. In no event shall the Royal Society of Chemistry be held responsible for any errors or omissions in this *Accepted Manuscript* or any consequences arising from the use of any information it contains.

Influence of yttrium dopant on the properties of anatase nanoparticles and the performance of dye-sensitized solar cells

Bingxin Zhao, Jinshu Wang^{*}, Hongyi Li^{*}, Hong Wang, Xinjian Jia and Penglei Su

Key Laboratory of Advanced Functional Materials, College of Materials Science and Engineering, Beijing University of Technology, Beijing 100124, P. R. China

Reprint Author: wangjsh@bjut.edu.cn, lhy06@bjut.edu.cn

Tel & Fax: +8610-67391101

Abstract: TiO₂ mesoporous nanoparticles (*NPs*) doped with yttrium (Y) ions are fabricated via an environmentally friendly and facile solvothermal method to serve as photoanode for dye sensitized solar cells (*DSSCs*). X-ray diffraction, X-ray photoelectron spectroscopy, transmission electron microscopy and N₂ adsorption–desorption tests are used to characterize the influence of yttrium dopant on the properties of TiO₂ *NPs*. The prepared Y–doped TiO₂ *NPs* have anatase phase and exhibit Ti–O–Y bonds. The photovoltaic performance is primarily associated with the morphological parameters of the *NPs*. At the optimum Y concentration of 3 at%, the short circuit current density has increased from 13.20 to 15.74 mA·cm⁻², full sun solar power conversion efficiencies increased from 6.09% up to 7.61% as compared to the blank *DSSC*.

Key words: titanium dioxide; rare earth; mesoporous structure; specific surface area; photovoltaic performance

1. Introduction:

Dye-sensitized solar cells (*DSSCs*), invented by Grätzel [1], were designed as a sandwich structure which contains a photoanode, an electrolyte and a counter electrode. Over the last decade, the photoanode has been targeted with numerous efforts. Among these components, the photoanode not only transports photo-induced electrons but also acts as the matrix to adsorb organic dyes, which directly determines the photo-current density [3]. Among various candidates, TiO_2 has been identified as a promising photoanode material and has been widely investigated [3–5]. Generally, to effectively adsorb dyes, a large specific surface area (*SSA*) is necessary [6]; therefore, various technologies have been developed to enlarge the *SSA*, such as micelle [7,8], block copolymer [9] and ordered templates [10]. Unfortunately, all those approaches need post-processing [11,12], which retard their application. Therefore, it is highly desirable to find a facile way to enlarge the *SSA* of TiO_2 nano-powders. Mesoporous structure may be an option, not only offering higher surface area (providing sites for adsorbing organic dyes), but also possessing linked walls for the diffusion of photo-induced electrons.

Rare earth elements (*REEs*) have been employed extensively in photocatalysis [13–15] and selective catalytic reduction [16] to improve the electron-hole (*e-h*) separation and to narrow the optical band gap for light harvesting of semiconductors [17–22]. Typically, researchers synthesized TiO_2 with Y doping and revealed that Y doping was helpful to the formation of oxygen vacancies for NO oxidation [16] and photocatalysis [17]. Besides, the role of *REEs* in *DSSC* photoanodes has been discussed in several other publications [23–26]. Light harvesting enhancement by dye

adsorption or other ways and electron transport improvement are major aims to incorporate *REEs* into *DSSCs*. Oh et al. [23] synthesized a Eu(III)-complex as an ultraviolet (*UV*) light-harvesting coadsorbent of *DSSC* and obtained a high short circuit photocurrent densities (J_{SC}) of 17.72 mA/cm² while that of the reference *DSSC* was 15.53 mA/cm². G. B. Shan [24] synthesized Er³⁺/Yb³⁺ co-doped LaF₃-TiO₂ nanocomposite and applied it as external up-conversion layer in the photoelectrode to harvest near infrared (*NIR*) light, improving the photocurrent with 2.4%. Zalas and Klein [25] fabricated TiO₂ films with lanthanide ions and reported that the *RE*-containing layer might act as an energy barrier preventing electron back-transfer. Zhang et al. [26] increased the density of oxygen vacancies of TiO₂ surface for dye adsorption by La doping and provided a power conversion efficiency (*PCE*) of 6.72%, which was a 13.5% improvement compared with that of references cell. However, to the best our knowledge, no report on mesoporous structure particles with *REE* doping for *DSSC* has been found. As is known, Y(III) has one occupied 4d orbital, which easily produces several electron configurations [27]. Besides, Y has the smallest ionic radius among *REEs* [28], which is relatively close to the Ti⁴⁺ radius, thus, the substitution of Ti by Y seems feasible. Hence, in the present work, Y was adopted as the dopant, and the irregular mesoporous structure of the nano-powders was achieved via a facile way. The effect of irregular mesoporous structure by Y doping TiO₂ was reflected in the enhanced performance of *DSSCs*, which may open the way for further photoanode material research in *DSSCs* field.

2. Experimental

2.1. Preparation of Y-doped TiO₂ powders:

Y-doped TiO₂ nanoparticles (NPs) were synthesized by modifying the reported method for blank TiO₂ NPs [29]. A stock solution of Ti⁴⁺ (0.5 M) was prepared by mixing titanium isopropoxide (TTIP) and triethanolamine (TEOA) (1 M), followed by adding distilled water. A small amount of yttrium nitrate (Y(NO₃)₃·6H₂O) was initially added into the above mixture (Y³⁺/Ti⁴⁺ molar ratio= 0.6 at%, 1.8 at%, 3.0 at%, 4.2 at% and 5.4 at%, and TTIP:TEOA molar ratio = 1:2). The mixture was transferred into a Teflon-lined autoclave, aged at 100 °C for 24 h to get gelation (the first aging). Then, the second aging treatment was performed at 140 °C for 72 h to nucleate and grow TiO₂ particles doped with Y ions. The obtained Y-doped TiO₂ powders were assigned as X%Y-TiO₂, where X represents the initial molar ratio of Y/Ti as determined by the weighed quantities of TTIP and yttrium nitrate. The molar ratio in the NPs can deviate from this initial ratio. For comparison, pure TiO₂ was prepared using the same procedure without Y³⁺. TTIP hydrolysates were identified as amorphous TiO₂ using the transmission electron microscope (TEM) in combination with selected area electron diffraction (SAED), as shown in Fig. S1. The SAED pattern indicated that TiO₂ was in the amorphous state before further heat treatment.

2.2 Photoanode preparation:

The pastes (Y-doped or not), made from the above powders, were deposited on the surface of fluorine-doped tin oxide (FTO) conductive glass using the doctor blade technique (FTO, sheet resistance: 15 Ω). The film thickness could easily be tailored by tuning the paste's viscosity and the depositing time. The deposited films were dried

at 130 °C and subsequently annealed at 500 °C for 1 h in air to remove residual organic compounds as well as to improve the bonding between the TiO₂ film and the FTO substrate. The annealed samples were immersed into a solution containing 40 mM TiCl₄ for 30 min at 70 °C, rinsed using deionized water, and then sintered at 500 °C. Finally, the film was dipped into an acetonitrile and ethanol (volume ratio=2:1) solution containing 0.5 mM cis-bis (isothiocyanato) - bis (2,2'-bipyridyl-4,4'-dicarboxylato) -ruthenium(II) -bis-tetrabutyl-ammonium (N719) dye, and kept at room temperature for 24 h.

2.3. Y-doped TiO₂ nanoparticles characterizations and photovoltaic performance

The morphology of the obtained samples was studied using a transmission electron microscope (TEM) (HitachiH-700). The crystal structure of the specimen was identified by X-ray diffraction (XRD) using a Bruker D8 advance diffractometer with Cu K α radiation. The N₂ adsorption-desorption tests were measured using micromeritics ASAP 2020 at 77 K with N₂ physical adsorption, temperature-programmed reduction/desorption (TPR/TPD) and Mossbauer effect spectroscopy (MES) methods. The specific surface area (SSA) was calculated based on the Brunauer-Emmett-Teller (BET) method. Desorption pore volume (for pores of diameter 1.7–300 nm) and pore width, measured by the Barrett-Joyner-Halenda (BJH) method. X-ray photoelectron spectrum (XPS) measurements were performed on a thermo scientific X-ray photoelectron spectroscopy made in UK (ESCALAB 250Xi). The XPS binding energy (BE) was internally referenced to the C 1s peak ($w = 285$ eV). The adsorbed dye of the photoanode was desorbed in a mixed solution of water and

ethanol (volume ratio = 1:1) containing 0.1 M NaOH, and then measured with an *UV-Vis* spectrometer (SHIMADZU, UV-2550). The current-voltage (*I-V*) measurements were performed on a Keithley 2400 power source under irradiation of 1 Sun whose intensity of the incident light was air mass (*AM*) 1.5 G. This instrument was equipped with a 300 W solar simulator (Solar Light Co., INC.), which served as the light source. In order to gain better understanding of the electrical properties, the electrochemical impedance spectrum (*EIS*) was recorded under light irradiation via an electrochemical workstation (Zahner, IM6ex).

3. Results and Discussion:

3.1. Investigation of pure and doped nanoparticles

Figure 1 shows the *XRD* diffraction pattern of pure TiO₂ and X%Y-TiO₂. It is clear that, according to *JCPDS* 65-5714, the as-prepared pure TiO₂ and X%Y-TiO₂ nanoparticles (*NPs*) are in the anatase phase. However, the diffraction peak of sample X%Y-TiO₂ is obviously broader, besides, the peak intensities of the X%Y-TiO₂ are weaker than those found for pure TiO₂, which can possibly be attributed to the presence of foreign ions in the crystal lattice [30]. As depicted in Fig. S2, small shifts in peaks are observed reflecting an expansion of the unit cell volume. The lattice parameters and the unit cell volumes of pure TiO₂ and X%Y-TiO₂ are calculated from equation for tetragonal system:

$$d_{hkl} = \frac{1}{\sqrt{\frac{h^2 + k^2}{a^2} + \frac{l^2}{c^2}}} \quad (1)$$

Where d_{hkl} is the interplanar spacing, which is determined from the anatase diffraction peaks of 101 and 200 for pure TiO_2 and $X\%Y\text{-TiO}_2$. As shown in Table 1, a universal trend of the elongation of each axis and increase of unit cell volume are observed with the increase of the Y concentration. When the initial Y molar ratio is 3%, the lattice volume expands from 137.35 \AA^3 (non doped *NPs*) to 138.30 \AA^3 . The expansion of the TiO_2 lattice may be attributed to the difference in ionic radii of Y^{3+} (0.089 nm) and Ti^{4+} (0.068 nm), which indicates that the Y ions are incorporated into TiO_2 lattice. Besides, the crystallite size (D) is determined from Debye–Scherrer equation:

$$D = \frac{k\lambda}{\beta \cos \theta} \quad (2)$$

Where λ is the CuK X-ray wavelength (1.5406 \AA), k is a constant (in this study $k=0.943$), β is the full-width at half maximum (*FWHM*) and θ is the diffraction angle. The general observation from the data shown in Table 1 is that smaller crystallite size is obtained in all Y-doped samples. Obviously, 3%Y- TiO_2 *NPs* exhibit the smallest average size of 25.11 nm (that of non doped *NPs* is 28.41 nm). Upon further increasing the Y doping concentration, the Y-doped samples show a tendency for larger particle sizes again. M. Khan et al. [14] fabricated Y doped anatase using hydrothermal method which exhibited a reduced particle size and larger *BET* specific surface area compared to bare TiO_2 . Besides, L. Cheng et al. [31] synthesized Y doped SnO_2 by the electro-spinning method and suggested that Y doping distorts the crystal lattice and subsequently prevents the growth of crystallites. Since smaller particles

usually manifest larger specific surface area (*SSA*), this is in good accordance with the relationship between our particle size and *SSA* results as indicated in Table 1.

X-ray photoelectron spectrum (*XPS*) is adopted to further investigate the chemical state of the elements and explore how the doped yttrium cations interact with TiO_2 . The results are summarized in Fig. 2. Fig. 2a depicts the full scan *XPS* spectra of binding energy (*BE*). In Fig. 2b, the peak position of the O 1s core levels of 3%Y- TiO_2 shifts to higher energy compared with those of undoped TiO_2 , indicating that the chemical environment of the elements has been changed. [32,33] Further, the O1s spectrum shows that two different oxygen binding energies exist in the as-prepared Y doping TiO_2 , as compared with the binding energy of oxygen in pure TiO_2 . The O1s peak of 3%Y- TiO_2 is divided into two different peaks which are located at 529.49 and 530.32 eV. These can be attributed to Ti-O and Y-O binding energy, respectively, as compared to that of pure TiO_2 shown in Fig.2b and Y-O binding energy in the literature (529.5 eV). [33] The spectrum for the Y 3d region of 3%Y- TiO_2 is shown in Fig. 2c. The *BE* of Y $3d_{5/2}$ and Y $3d_{3/2}$ for 3%Y- TiO_2 is about 157.58 and 159.63 eV, respectively, with a spin-orbit splitting of 2.05 eV. These results are giving the evidence that the oxidation state of the Y ions is mainly trivalent. [34] Since oxidized yttrium was not observed in the *XRD* diagrams of X%Y- TiO_2 although the concentration of Y is more than 3 at% (as shown in Fig. 1), it is certain that some Y ions have been successfully substituted Ti ions in the TiO_2 lattice during the solvothermal process, and some Ti-O bonds in pure TiO_2 shown in Fig. 2b have

been replaced by Y–O bonds. Besides, the *XPS* analysis result indicates that the actual Y amount in 3%Y–TiO₂ is 1.21 at%.

The *TEM* study was done to examine the effect of Y doping on the morphology of anatase, as shown in Fig. 3. The average particle size of the *NPs* is 10–40 nm, which is in agreement with the average value of the crystallite size determined by *XRD* (as shown in Table 1). As shown in Fig. 3b and Fig. 3e, in contrast to the regular structure of pure TiO₂ *NPs*, 3%Y–TiO₂ *NPs* possess a more irregular mesoporous structure. The accumulated 3%Y–TiO₂ *NPs* with irregular structure (see Fig. 3e) have an enhanced surface area and linked framework that will facilitate the diffusion of photo-induced electrons. The Selected area electron diffractions (*SAED*) shown in insets of Fig. 3a and 3d clearly indicate the poly-crystallinity circles in anatase of TiO₂ and 3%Y–TiO₂. Fig. 3c and 3f show that (101) planes have slightly expanded in 3%Y–TiO₂ (3.46 Å) compared to those in pure TiO₂ (3.45 Å). This agrees favorably with the 101 interplanar spacing calculated from 101 diffraction angle of TiO₂ and 3%Y–TiO₂ (see Table S2), indicating also that Y ions have been doped into the TiO₂ lattice. Finally, by comparing the microstructure of pure TiO₂ (Fig. 3g) with that of 3%Y–TiO₂ (Fig. 3h), lattice distortion can be detected, indicating oxygen vacancy and substitution of Y for Ti in 3%Y–TiO₂ lattice. In other words, the *XRD*, *XPS* and *TEM* analysis results indicate that Y ions have entered into the TiO₂ lattice and substituted Ti sites.

The N₂ adsorption–desorption isotherms and pore size distributions of pure and doped nanoparticles are recorded and depicted in Fig. 4. It is shown in Fig. 4a that the

isotherms of TiO_2 and $X\%Y\text{-TiO}_2$ are identified as type V, a typical characteristic of mesoporous materials according to the International Union of Pure and Applied Chemistry (*IUPAC*) classification system. The pore size distribution (Fig. 4b) of $3\%Y\text{-TiO}_2$ ranges from 5 to 48 nm, which is broader than that of TiO_2 (5 to 35 nm). The hysteresis loop appears to be type H2, indicating that the pores are formed by accumulated *NPs* due to the high surface activity of the as-prepared *NPs*. Effects of Y doping on the *BET* surface area and pore parameters are summarized in Table 1. The mesoporous *NPs* with 3 at% dopant offer a high specific surface area and a pore volume of $142 \text{ m}^2/\text{g}$ and $0.564 \text{ cm}^3/\text{g}$, respectively, being 36.6% and 121.5% higher than that of pure TiO_2 *NPs*. An increase of *SSA* and pore volume in the sequence $3\%Y\text{-TiO}_2$ - $1.8\%Y\text{-TiO}_2$ - $0.6\%Y\text{-TiO}_2$ - TiO_2 is observed, while a large decrease in $4.2\%Y\text{-TiO}_2$ and $5.4\%Y\text{-TiO}_2$ occurs. However, all *NPs* with Y doping have higher *SSA* and pore volume compared with reference sample. The smaller size (see Table 1) and irregular structure (see Fig. 3e) in doped *NPs* may account for the increase of *SSA* and pore volume for block $X\%Y\text{-TiO}_2$. TiO_2 powders with higher *SSA* and larger pore volumes can enhance the efficiency of *DSSC* because more surface sites are available to adsorb organic dye, resulting in the enhancement of light harvest capability and increasing the amount of excited electrons, which move through the interconnected porous network.

3.2. Photovoltaic performance

The characteristic current–voltage (*I–V*) curves for pure and Y-doped TiO_2 and the effect of Y/Ti molar ratios on the relationship between specific surface area and

conversion efficiency are depicted in Fig. 5. The detailed photovoltaic parameters, including energy conversion efficiency, open-circuit voltage (V_{OC}), fill factors (FFs) and short circuit photocurrent densities (J_{SC}) are summarized in Table 2. The dye adsorption has been measured and is also listed in Table 2: the amount of dye increased as the SSA increased. The SSA substantially enhances the dye adsorption from 0.79×10^{-7} (pure) to 1.26×10^{-7} mol/cm² (3%Y-TiO₂). Clearly, compared with the pure TiO₂ based $DSSC$, a general increase of J_{SC} has been observed for the X%Y-TiO₂ based $DSSC$. In addition, we also measured the incident photo-current efficiency ($IPCE$) spectra of the pure and X%Y-TiO₂ based $DSSCs$ as shown in Fig. S4. The $IPCE$ results are consistent with the photocurrent of the $DSSCs$. As shown in Fig. 5b, the irregular structure and small particle size due to the Y incorporation into the TiO₂ matrix could provide high SSA and thus increase the amount of excited electrons because of larger dye-adsorption, leading to the enhancement of J_{SC} . The highest J_{SC} value (15.74 mA/cm²) has been achieved by 3%Y-TiO₂ based $DSSC$. Further increasing Y/Ti molar ratios over 4.2% leads to J_{SC} reduction, which can be attributed to a larger internal resistance [26]. Furthermore, a red shift of the absorption edge is observed in the $UV-Vis$ absorption spectra of TiO₂ and Y-doped TiO₂ (Fig. S3). The absorption threshold shifts from 395 nm (undoped) to 405 nm (3%Y-TiO₂); so, the optical band gap decreases from 3.14 eV to 3.06 eV (see Table 1). The probable reason is that Y doping induces a part of the Y 4d states to extend into the TiO₂ conduction band resulting into narrowing of the band gap of anatase [14,35]. This may promote the transport of electrons. As listed in Table 2, Y doping also

results in a slight increase of V_{OC} , which may be due to a small upward shift of the *Fermi* level upon Y doping [35], since the voltage produced under illumination corresponds to the difference between the electrons in the *Fermi* level of TiO_2 NPs and the chemical potential of the holes in the hole conductor (electrolyte). [36] It should be noted that Y doped TiO_2 DSSC devices have higher fill factor (*FF*) values. The *FF* reflects the quality of the TiO_2 film and the external electrical and electrochemical losses during the operation of the DSSCs [37,38]. The N_2 absorption-desorption measurement, *BET*, dye amount, *I-V* characteristics curves jointly demonstrate that the doping of Y plays an important role in the *SSA*, dye adsorption and the efficiency of DSSCs (see Table 2).

To study the difference between the interfacial characteristics of the photo-electrodes, the electrochemical impedance spectra (*EIS*) of DSSCs based on pure TiO_2 and X%Y- TiO_2 have been measured in a frequency range from 0.01 Hz to 3 MHz under simulated solar light with an intensity of 100 mW/cm^2 (*AM 1.5*). Results are shown in Fig. 6. According to Quintana et al. [39], the hemisphere in the intermediate-frequency region represents the transport resistance (R_{ct}) associated with the charge transfer across the TiO_2 film and the TiO_2 /redox electrolyte interface. Experimental data have been fitted to the model as depicted in Fig. 6c represented by the equivalent circuit. The *EIS* parameters of the TiO_2 and X%Y- TiO_2 based DSSCs are listed in Table 2. A decrease of R_{ct} in the sequence TiO_2 - 0.6%Y- TiO_2 - 1.8%Y- TiO_2 - 3%Y- TiO_2 is observed, while an increase occurs when the initial Y molar ratio is over 4.2%, which is consistent with the J_{SC} and the energy conversion

efficiency of the obtained solar cells. S. Phadke et al. [40] explained the *EIS* of *DSSCs* in terms of electron transport energetics/kinetics of the photoelectrochemical processes and the pore-channel openness and interconnection of the photoanode. They proved that the incorporation of a hierarchical, interconnected network of pores in the TiO_2 electrode improves the charge transport. As shown in Table 2, the larger transport resistance of TiO_2 based *DSSC* as compared to that of $\text{X}\%\text{Y-TiO}_2$ based *DSSC* can be due to the linked and irregular mesoporous structure of the latter: this enhances the diffusion of photo-induced electrons (see Fig. 3). In addition, the electron lifetime (τ_e) can be calculated from the Bode plots (Fig. 6b), using the following equation:

$$\tau_e = \frac{1}{2\pi\omega_{\max}} \quad (3)$$

Where ω_{\max} is the frequency at which the intermediate-frequency peak appears in the Bode plot. Table 2 summarizes ω_{\max} , τ_e and R_{ct} of TiO_2 and $\text{X}\%\text{Y-TiO}_2$. The τ_e value first increases to 20.47 ms and then decreases. Among these cells, 3%Y- TiO_2 cell has the highest τ_e value (20.47 ms) and lowest R_{ct} value (19.38 Ω), resulting in the highest efficiency of energy conversion. It can be deduced from the *EIS* results that Y doping is prolonging the lifetime of the injected electron and reduces the charge transport resistance significantly: hence, it improves the photovoltaic performance of the solar cell. From the results mentioned above, we conclude that a small particle size and irregular mesoporous structure caused by the Y incorporation into the TiO_2 matrix is responsible for the high τ_e , the low R_{ct} , the high V_{OC} , the high J_{SC} , the high *FF* and therefore the higher conversion efficiency of $\text{X}\%\text{Y-TiO}_2$ based *DSSCs*.

4. Conclusion:

Mesoporous Y-doped TiO₂ nanoparticles (*NPs*) have been successfully synthesized via a facile strategy. Y doping leads to smaller particle size and expansion of the TiO₂ lattice compared with the reference sample. Transmission electron microscopy indicates the linked and irregular mesoporous structure for the photo-induced electron diffusion of doping *NPs*. It is found that a Y doping concentration of 3 at% yields the best performance in terms of short circuit current density and efficiency. The parameters that correlate best with this performance increase are the specific surface area, the pore volume, the electron lifetime and the transport resistance. A *DSSC* with mesoporous 3%Y-TiO₂ *NPs*, which have the highest specific surface area and pore volume (being 36.6% and 123% higher than that of pure TiO₂), demonstrates ~53% decrease of transport resistance and ~216% increase of electron lifetime compared with the reference *DSSC*. Such doping effectively improves the photocurrent from 13.20 to 15.74 mA·cm⁻², photovoltage from 703 to 706 mV, yielding a high energy conversion of 7.61%. Finally, we hope that the present work is a good starting point for understanding the properties of mesoporous Y-doped *NPs* and *DSSCs*. We intend to study the electronic behavior related to the morphology of doped photoanode in *DSSCs*, both experimentally and theoretically.

Acknowledgements

This work is financially supported by National Natural Science Foundation of China (51471006, 51225401), Beijing Natural Science Foundation (No. 2151001) and Guangxi Natural Science Foundation (2014GXNSFB118001).

References

- [1] B. O'Regan, M. Grätzel, *Nature*, 1991, **353**, 737–740.
- [2] C. K. Dong, W. C. Xiang, F. Z. Huang, D. C. Fu, W. C. Huang, U. Bach, Y. B. Cheng, X. Li, L. Spiccia, *Nanoscale* 2014, **6**, 3704–3711.
- [3] H. Wang, M. Liu, M. Zhang, P. Wang, H. Miura, Y. Cheng and J. Bell, *Phys. Chem. Chem. Phys.*, 2011, **13**, 17359–17366.
- [4] Q. Zhang, D. Myers, J. Lan, S. A. Jenekhe and G. Cao, *Phys. Chem. Chem. Phys.*, 2012, **14**, 14982–14998.
- [5] E. L. Unger, S. J. Fretz, B. Lim, G. Y. Margulis, M. D. McGehee and T. D. P. Stack, *Phys. Chem. Chem. Phys.*, 2015, **17**, 6565–6571.
- [6] R. Katoh, A. Furube, *J. Photoch. Photobio. C*, 2014, **20**, 1–16.
- [7] A. Leonard, J. L. Blin and B. L. Su, *Chem. Commun.*, 2003, **20**, 2568–2569.
- [8] Z.Y. Yuan, A. Vantomme, A. Leonard and B. L. Su, *Chem. Commun.* 2003, **13**, 1558–1559.
- [9] A. Sarkar, N.J. Jeon, J. H. Noh and S. Seok, *J. Phys. Chem. C*, 2014, **118**, 16688–16693.
- [10] D. A. Erdogana, M. Polata, R. Garifullin, M. O. Guler and E. Ozensoy, *Appl. Surf., Sci.* 2014, **308**, 50–57.
- [11] J.S. Wang, H. Li, H.Y. Li, C. Zou, H. Wang, and D. Li, *ACS Appl. Mater. Interfaces* 2014, **6**, 1623–1639.
- [12] J.S. Wang, H. Li, H.Y. Li, H. Wang and Q. Cai, *J. Nanosci. Nanotechno.* 2013, **13**, 1493–1497.

- [13] X.C. Zhang, H.M. Yang and A.D. Tang, *J. Phys. Chem. B*, 2008, **112**, 16271–16279.
- [14] M. Khan and W.B. Cao, *J. Appl. Phys.*, 2013, **114**, 183514–183517.
- [15] W. J. Zhang, K. L. Wang, S. L. Zhu, Y. Li, F. Wang and H. He, *Chem. Eng. J.* 2009, **155**, 83–87.
- [16] S. L. Zhang, X. X. Liu, Q. Zhong and Y. Yao, *Catal. Commun.* 2012, **25**, 7–11.
- [17] H. Zhang, K. Tan, H. Zheng, Y. Gu, W. F. Zhang, *Mater. Chem. Phys.*, 2011, **125**, 156–160.
- [18] A.W. Xu, Y. Gao and H. Q. Liu, *J. Catal.* 2002, **207**, 151–157.
- [19] C. Liang, C. Liu, F. Wu and F. Wu, *Chem. Eng. J.*, 2009, **147**, 219–225.
- [20] J. Shi, J. Zheng, and P. Wu, *J. Hazard. Mater.*, 2009, **161**, 416–422.
- [21] W. Smith, S. Mao, G. Lu, A. Catlett, J. Chen and Y. Zhao, *Chem. Phys. Lett.*, 2010, **485**, 171–175.
- [22] C. M. Fan, P. Xue and Y. P. Sun, *J. Rare Earths*, 2006, **24**, 309–313.
- [23] H. O. Jung, M. S. Hae, K. E. Yu, H. R. Jung, J. J. Myung and K. K. Hwan, *Bull. Korean Chem. Soc.*, 2011, **32**, 2743–2750.
- [24] G. B. Shan and G. P. Demopoulos, *Adv. Mater.*, 2010, **22**, 4373–4377.
- [25] M. Zalas. and M. Klein, *Int. J. Photoenergy*, 2012, **2012**, 1–8.
- [26] J. Zhang, Z. Zhao, X. Wang, T. Yu, J. Guan, Z. Yu, Z. Li and Z. Zou, *J. Phys. Chem. C*, 2010, **114**, 18396–18400.
- [27] T. M. Su, Z. Z. Qin and H. B. Ji, *Phys. Rev. B*, 1997, **56**, 14993–15000.

- [28] P. Ramakul, T. Supajaroon, T. Prapasawat, U. Pancharoen and A. W. Lothongkum, *J. Ind. Eng. Chem.*, 2009, **15**, 224–228.
- [29] T. Sugimoto, X. P. Zhou and A. Muramatsu, *J. Colloid Interface Sci.* 2003, **259**, 43–52.
- [30] S. N. R. Inturi, T. Boningari, M. Suidan, P. G. Smirniotis, *Appl. Catal. B*, 2014, **144**, 333–342.
- [31] L. Cheng, S. Y. Ma, X. B. Li, J. Luo, W. Q. Li, F. M. Li, Y. Z. Mao, T. T. Wang and Y. F. Li, *Sensor. Actuat. B*, 2014, **200**, 181–190.
- [32] B. Xin, L. Jing, Z. Ren, B. Wang and H. Fu, *J. Phys. Chem. B*, 2005, **109**, 2805–2809.
- [33] X. Chen, L. Song, L. You and L. Zhao, *Appl. Surf. Sci.*, 2013, **271**, 248–252.
- [34] Y. Wu, Q. Zhang, X. Yin and H. Cheng, *RSC Adv.*, 2013, **3**, 9670–9676.
- [35] Matiullah Khan, Wenbin Cao and Mis hkat Ullah, *Phys. Status Solidi B*, 2013, **250**, 364–369.
- [36] M. Grätzel, *Acc. Chem. Res.*, 2009, **42**, 1788–1798.
- [37] Z. Gao, Z. Wu, X. Li, J. Chang, D. Wu, P. Ma, F. Xu, S. Gao and K. Jiang, *CrystEngComm*, 2013, **15**, 3351–3358.
- [38] H. Hafez, M. Saif and M. S. A. Abdel-Mottaleb, *J. Power Sources*, 2011, **196**, 5792–5796.
- [39] M. Quintana, T. Edvinsson, A. Hagfeldt, and G. Boschloo, *J. Phys. Chem. C* 2007, **111**, 1035–1041.

[40] S. Phadke, A. D. Pasquier and D. P. Birnie, *J. Phys. Chem. C* 2011, **115**, 18342–18347.

Table 1 The detail parameters of obtained pure and X%Y-TiO₂ NPs

| Sample | | TiO ₂ | 0.6%Y-TiO ₂ | 1.8%Y-TiO ₂ | 3%Y-TiO ₂ | 4.2%Y-TiO ₂ | 5.4%Y-TiO ₂ |
|---|-------------------------------|-----------------------|------------------------|------------------------|-----------------------|------------------------|------------------------|
| Anatase lattice parameters | a=b (Å) | 3.794 | 3.796 | 3.796 | 3.796 | 3.797 | 3.797 |
| | c (Å) | 9.542 | 9.557 | 9.576 | 9.598 | 9.610 | 9.641 |
| | cell volume (Å ³) | 137.35 | 137.71 | 137.99 | 138.30 | 138.55 | 138.99 |
| Average grain size (nm) | | 28.41 | 27.23 | 26.18 | 25.11 | 26.22 | 27.22 |
| Specific surface area (m ² /g) | | 87 | 101 | 136 | 142 | 113 | 111 |
| Pore size (nm) | | 11.50 | 10.80 | 11.53 | 15.81 | 11.57 | 12.02 |
| Pore volume (cm ³ /g) | | 2.53×10 ⁻¹ | 2.65×10 ⁻¹ | 3.96×10 ⁻¹ | 5.64×10 ⁻¹ | 3.30×10 ⁻¹ | 3.36×10 ⁻¹ |
| Absorption edge (nm) | | 395 | 400 | 400 | 405 | 399 | 399 |
| Band gap (eV) | | 3.14 | 3.10 | 3.10 | 3.06 | 3.10 | 3.10 |

Table 2 Detailed parameters of X%Y-TiO₂ based *DSSC* devices.

| <i>DSSC</i> Device | Film thickness (μm) | Photovoltaic performance | | | | | | | Amount of dye (mol/cm ² ×10 ⁻⁷) |
|------------------------|---------------------|-----------------------------|--|---------------|----------------|-----------------------|---------------------|----------------------------|--|
| | | <i>V</i> _{OC} (mV) | <i>J</i> _{SC} (mA/cm ²) | <i>FF</i> (%) | <i>Eff</i> (%) | ω _{max} (Hz) | τ _e (ms) | <i>R</i> _{ct} (Ω) | |
| TiO ₂ | 10.95 | 703 | 13.20 | 65.59 | 6.09 | 24.56 | 6.48 | 41.42 | 0.79 |
| 0.6%Y-TiO ₂ | 10.80 | 704 | 13.39 | 67.94 | 6.40 | 10.64 | 14.97 | 25.81 | 0.97 |
| 1.8%Y-TiO ₂ | 10.80 | 706 | 14.39 | 70.15 | 7.12 | 10.64 | 14.97 | 22.99 | 1.12 |
| 3%Y-TiO ₂ | 11.05 | 706 | 15.74 | 68.46 | 7.61 | 7.78 | 20.47 | 19.38 | 1.26 |
| 4.2%Y-TiO ₂ | 10.60 | 710 | 13.82 | 70.73 | 6.94 | 17.02 | 9.36 | 30.57 | 1.09 |
| 5.4%Y-TiO ₂ | 11.20 | 709 | 13.25 | 67.57 | 6.35 | 20.81 | 7.65 | 33.46 | 0.99 |

Figure Captions:

Fig. 1 *XRD* diffractogram of TiO_2 and X\%Y-TiO_2

Fig. 2 X-ray photoelectron spectroscopy spectra of TiO_2 and $3\%Y\text{-TiO}_2$ (a) Full scan *XPS* spectrum, (b) O 1s spectrum and (c) Y 3d core levels of $3\%Y\text{-TiO}_2$. For O 1s and Y 3d spectra the orange and grey lines are obtained by a curve fitting method.

Fig. 3 *TEM* images of TiO_2 (a, b, c and g) and $3\%Y\text{-TiO}_2$ (d, e, f and h) at different magnifications. *SAED* patterns from TiO_2 and $3\%Y\text{-TiO}_2$ nanoparticles are shown as inset in a, d.

Fig. 4 (a) N_2 absorption desorption isotherms of TiO_2 and X\%Y-TiO_2 powders (b) The corresponding pore size distribution curves

Fig. 5 (a) *I-V* curves of the *DSSC* devices based on pure TiO_2 and X\%Y-TiO_2 (b) Effect of Y/Ti molar ratios on the relationship between specific surface area and conversion efficiency. The insets are *TEM* images of bare TiO_2 and $3\%Y\text{-TiO}_2$ from Fig. 3.

Fig. 6 *EIS* spectra of TiO_2 and X\%Y-TiO_2 based *DSSCs*; (a) Nyquist plots, (b) Bode plots and (c) the equivalent circuit.

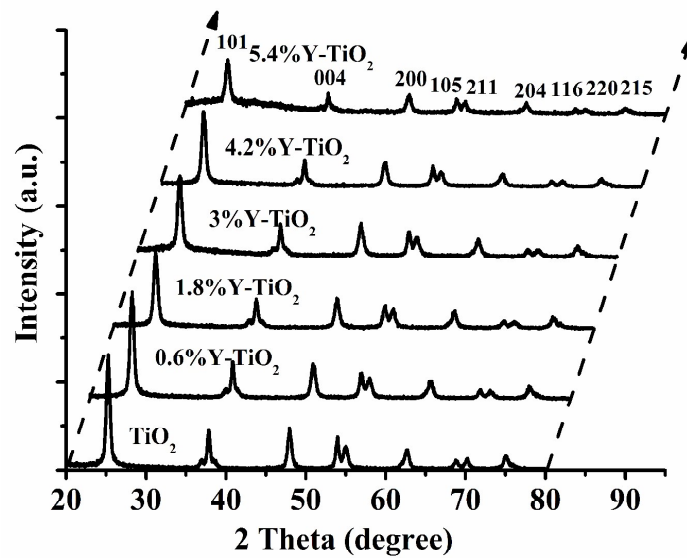


Fig. 1 XRD diffractogram of TiO_2 and X%Y- TiO_2

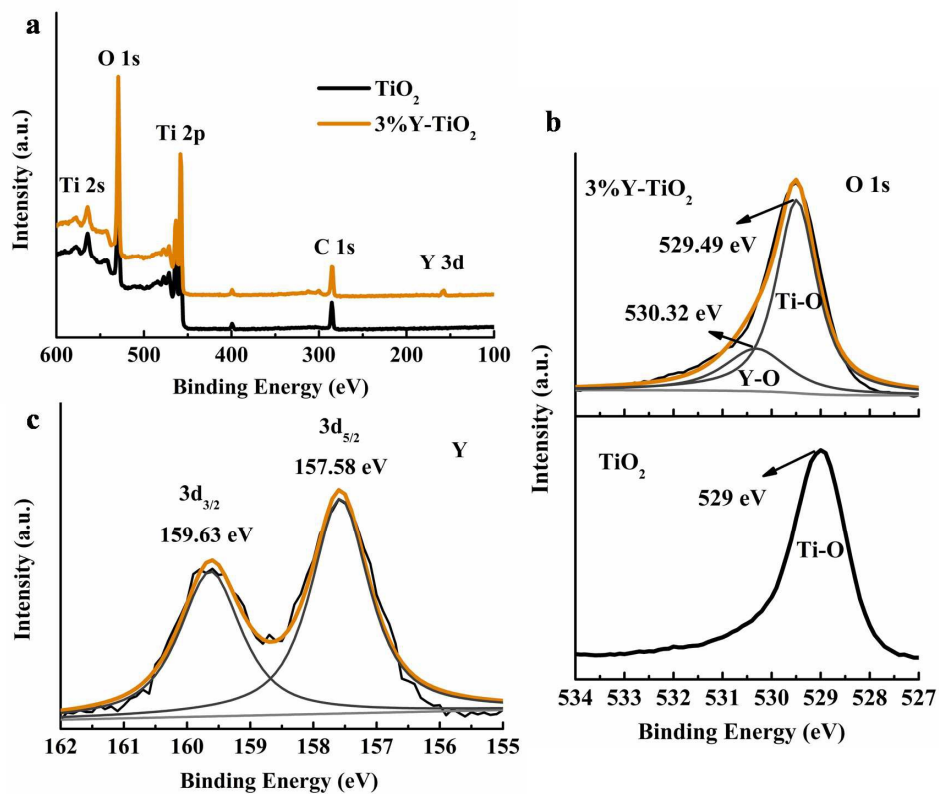


Fig. 2 X-ray photoelectron spectroscopy spectra of TiO_2 and 3%Y- TiO_2 (a) Full scan XPS spectrum, (b) O 1s spectrum and (c) Y 3d core levels of 3%Y- TiO_2 . For O 1s and Y 3d spectra the orange and grey lines are obtained by a curve fitting method.

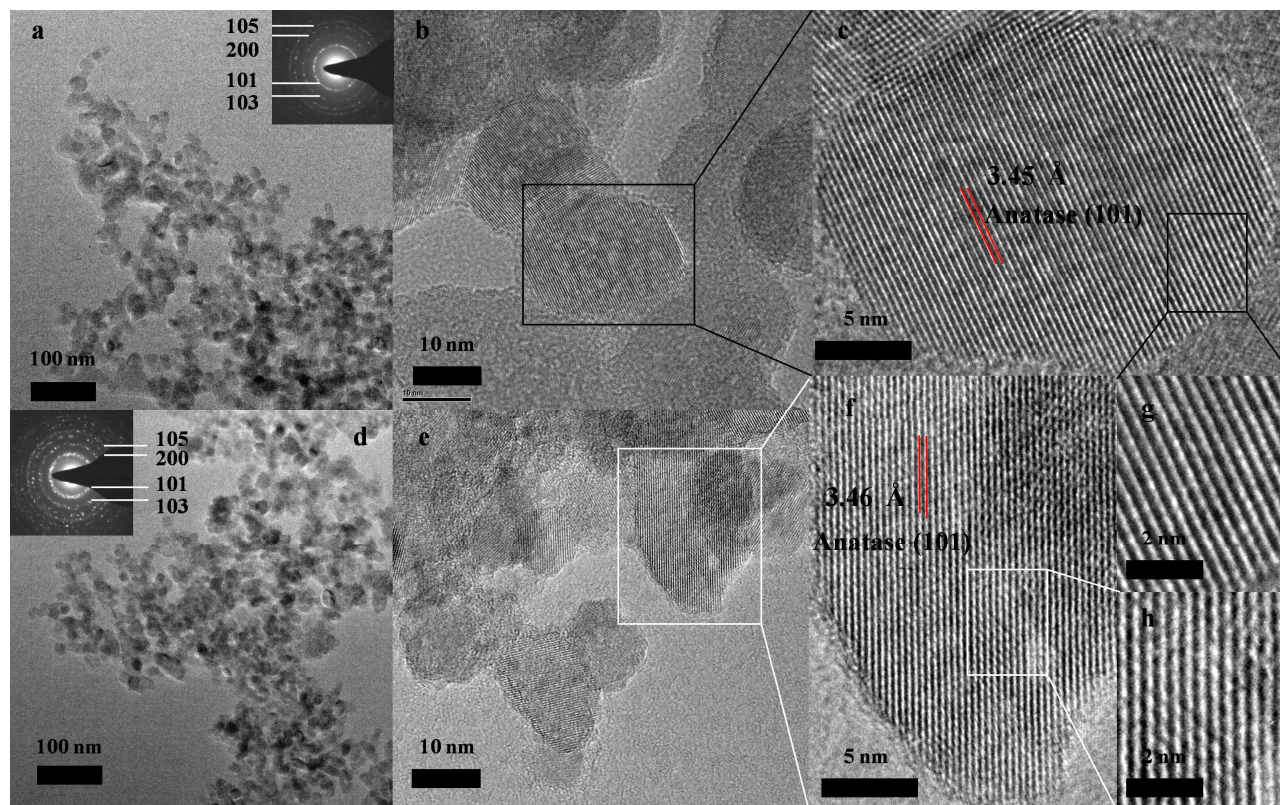


Fig. 3 TEM images of TiO₂ (a, b, c and g) and 3%Y-TiO₂ (d, e, f and h) at different magnifications. SAED patterns from TiO₂ and 3%Y-TiO₂ nanoparticles are shown as inset in a, d.

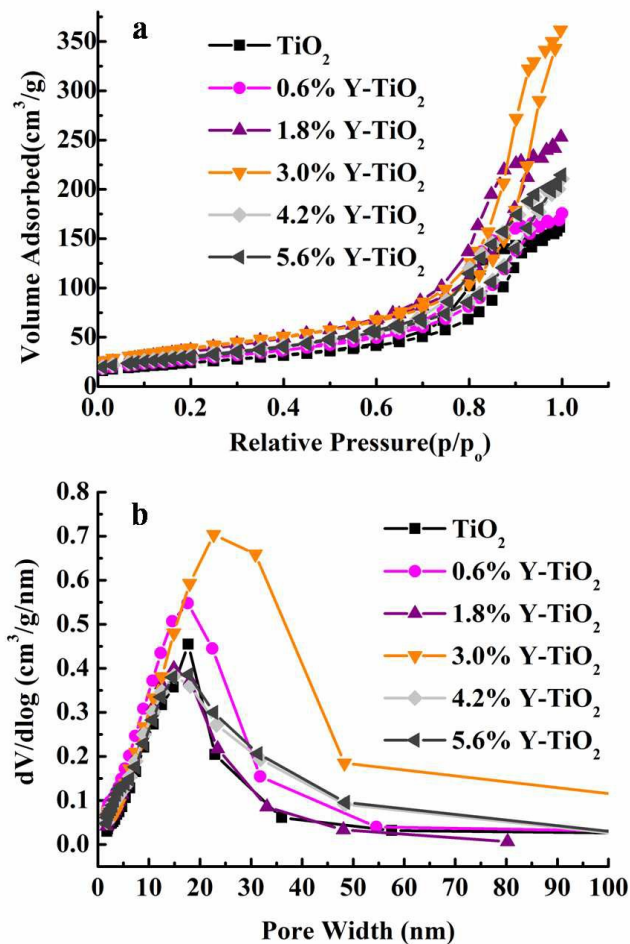


Fig. 4 (a) N₂ adsorption-desorption isotherms of TiO₂ and X%Y-TiO₂ powders (b) The corresponding pore size distribution curves

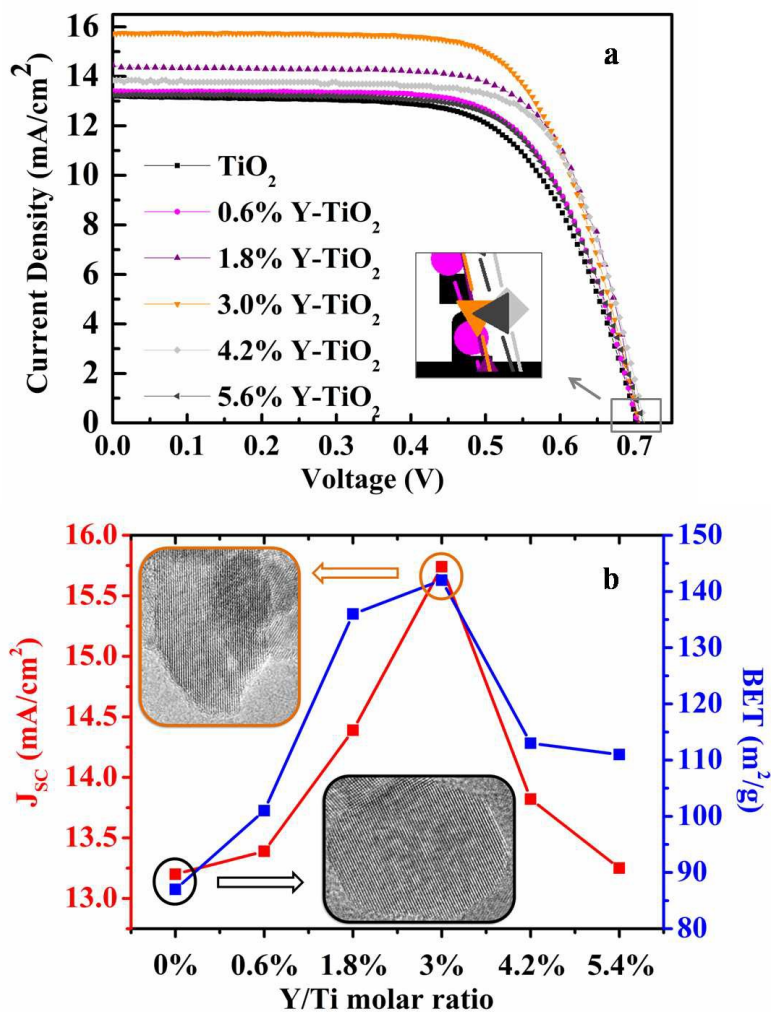


Fig. 5 (a) I - V curves of the $DSSC$ devices based on pure TiO_2 and $X\%Y-TiO_2$ (b) Effect of Y/Ti molar ratios on the relationship between specific surface area and conversion efficiency. The insets are TEM images of bare TiO_2 and $3\%Y-TiO_2$ from

Fig. 3.

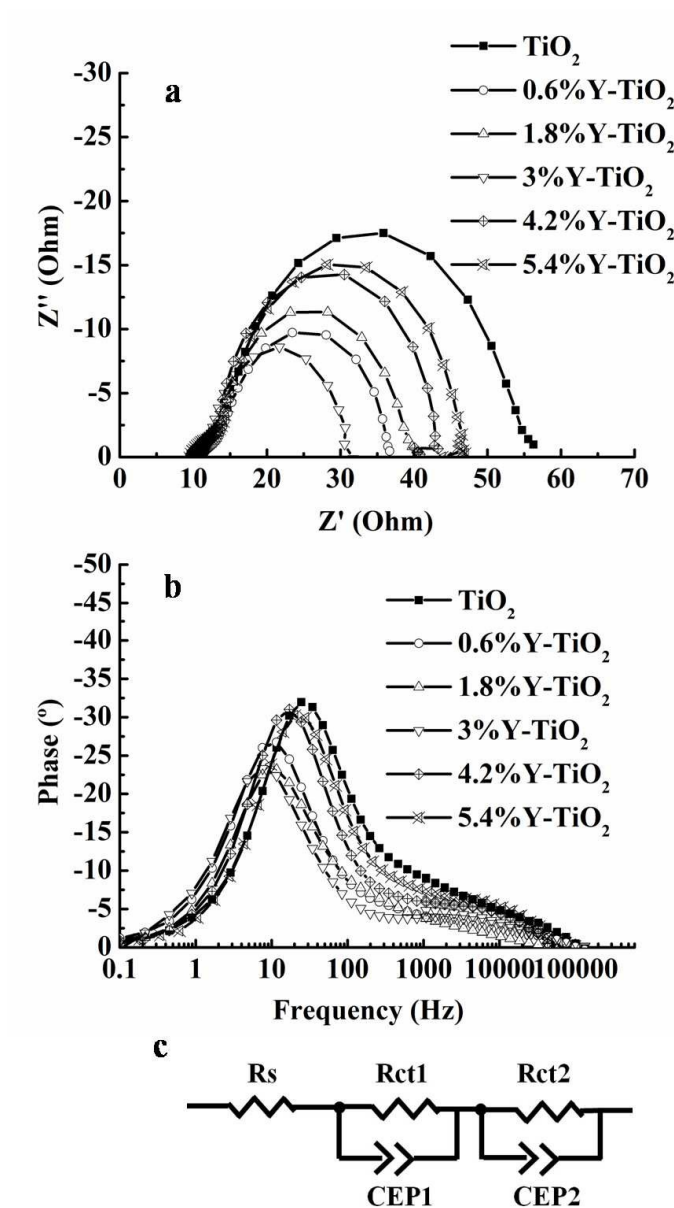


Fig. 6 EIS spectra of TiO_2 and $\text{X}\% \text{Y-TiO}_2$ based DSSCs; (a) Nyquist plots, (b) Bode plots and (c) the equivalent circuit.

Graphic Abstract

